

Modeling quark-hadron duality in polarization observablesSabine Jeschonnek¹ and J. W. Van Orden^{2,3}¹*Physics Department, The Ohio State University, Lima, Ohio 45804, USA*²*Jefferson Lab, 12000 Jefferson Ave, Newport News, Virginia 23606, USA*³*Department of Physics, Old Dominion University, Norfolk, Virginia 23529, USA*

(Received 25 January 2005; published 18 March 2005)

We apply a model for the study of quark-hadron duality in inclusive electron scattering to the calculation of spin observables. The model is based on solving the Dirac equation numerically for a scalar confining linear potential and a vector color Coulomb potential. We qualitatively reproduce the features of quark-hadron duality for all potentials considered, and discuss the onset of scaling and duality for the responses, spin structure functions, and polarization asymmetries. Duality may be applied to gain access to kinematic regions which are hard to access in deep inelastic scattering, namely, for $x_{Bj} \rightarrow 1$, and we discuss which observables are most suitable for this application of duality.

DOI: 10.1103/PhysRevD.71.054019

PACS numbers: 12.40.Nn, 12.39.Ki, 13.60.Hb

I. INTRODUCTION

Quark-hadron duality is a fascinating phenomenon that was first observed by Bloom and Gilman [1] more than 30 years ago. It is receiving plenty of attention today from both the experimentalist [2–10] and theorist [11–36] communities, due to an interest in duality itself, and due to the huge field of experimental applications of duality in kinematic regions that are very difficult to access without it.

The most straightforward definition of quark-hadron duality says that any hadronic process can be described in terms of either a quark and gluon picture, or in terms of a purely hadronic picture, provided either calculation contains all Fock states. However, in the former case, a full numerical solution of QCD is prohibitive in most situations, despite the impressive progress of lattice QCD, and in the latter case, a full hadronic solution, e.g., employing an effective field theory, also is not feasible unless the kinematic region is restricted to low energies and momenta. Thus, this most general version of duality is not very useful, as many interesting processes take place in a region that is neither perturbative nor very low energy.

There is a much more practical version of duality: in certain kinematic regimes, properly averaged hadronic observables can be described by a perturbative QCD (pQCD) calculation. This version of duality is highly relevant as perturbative QCD calculations can be performed. Using duality, these pQCD calculations can then be related to averaged data taken in the resonance region. Quark-hadron duality has been observed experimentally in many processes: it was discovered by Bloom and Gilman in inclusive, inelastic electron scattering, it made its way into the textbooks in $e^+e^- \rightarrow$ hadrons, was studied in the semileptonic decays of heavy mesons [37–39], is considered in the analysis of heavy ion reactions [40], and forms the basis for using QCD sum rules [41]. In addition to the “classical” examples and applications of duality, duality ideas are applied in new areas, too. For neutrino scattering, the beam energies are not well known, and an averaging

will thus take place almost automatically. The application of duality is discussed for several planned neutrino experiments, see e.g. [42], and duality ideas have been applied in Ref. [43] to nucleon/nuclear duality in neutrino scattering. There is also interest in duality in parity violation experiments [44], and with regard to generalized parton distributions [13,45]. A very local version of duality—assuming that it holds for just one resonance—has been used in Refs. [26,27] to extract information on structure functions at $x_{Bj} \rightarrow 1$ in the scaling limit from form factor data. These ideas were also applied to neutrino-nucleon scattering [27]. Duality ideas might also be useful for pion photoproduction [46]. Duality is a major point in the 12 GeV upgrade of Continuous Electron Beam Accelerator Facility (CEBAF) at Jefferson Lab [10].

In this paper, we investigate duality in inclusive, inelastic electron scattering. New experimental data from Jefferson Lab and Deutsches Elektronen Synchrotron (DESY) have impressively confirmed that quark-hadron duality is valid down to rather low four-momentum transfers, and for many observables: duality in F_2 was confirmed to hold down to $Q^2 \approx 0.5 \text{ GeV}^2$ [2], and very recently, the longitudinal structure function F_L and the purely transverse F_1 were separated, and found to exhibit duality for $Q^2 > 1 \text{ GeV}^2$ [3]. Experimental evidence for duality in spin observables has been reported for A_1^p from Hermes [7] and from Jefferson Lab [5] for the first moment of g_1^n . While this is exciting all by itself, these data have inspired experimentalists to apply duality to the extraction of information on the deep inelastic region in kinematics that are not readily accessible. Duality allows us to connect the perturbative regime of quarks and gluons with the strongly nonperturbative resonance regime. The earliest example discussed was the extraction of the elastic nucleon form factor from the deep inelastic scaling curve [47]. In Ref. [48], higher twist contributions were inferred from the resonance data.

These two kinematical regions have traditionally been separated, as it was believed that the physics of quarks and

gluons had little connection to the collective phenomena of resonances. At low invariant masses W of the final state in an (e, e') reaction on the nucleon, one observes many resonance bumps in the cross section, and $W < 2$ GeV is traditionally referred to as the resonance region. For higher invariant masses, $W > 2$ GeV, the cross section becomes smooth and exhibits Bjorken scaling, and this region is referred to as the deep inelastic region. Note that this strict division of kinematics was introduced historically, even though nonresonant processes are present for low W , and resonances with larger mass may contribute for high W . The demarcation line of $W = 2$ GeV is plotted in the $x_{\text{Bj}}-Q^2$ plane in Fig. 1.

One consequence of this traditional subdivision is that large amounts of data with $W < 2$ GeV were cut from deep inelastic analyses of data, leading to a paucity of data at very high Bjorken x_{Bj} . The region of large x_{Bj} , $x_{\text{Bj}} \rightarrow 1$, is referred to as the (deep) valence region, and is the subject of much interest. In particular, one would like to study the valence quark spin distribution of the nucleon. This can be achieved by measuring the polarization asymmetry A_1 of the proton and neutron. For $x_{\text{Bj}} \rightarrow 1$, many, and widely different predictions, exist for the polarization asymmetry of the neutron, running the gamut from 0, predicted in unbroken SU(6), to 1, predicted in pQCD, and everything in between, see [49,50] for good reviews of the situation. In the chiral soliton model, there are even predictions of negative values [51].

The experimental data available for A_1^n at high x_{Bj} was rather scarce and afflicted with very large error bars for $x_{\text{Bj}} > 0.4$ before the advent of the recent Jefferson Lab data

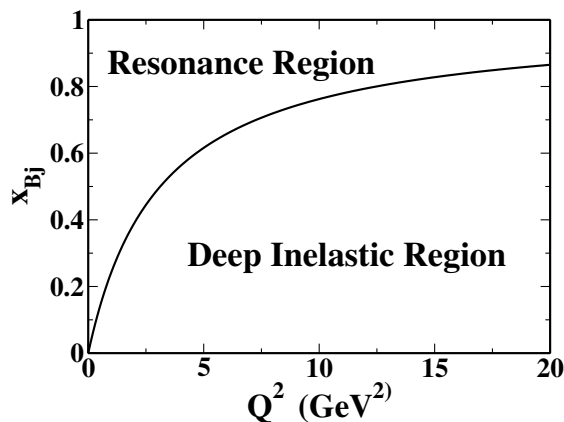


FIG. 1. Plot of the x_{Bj} and Q^2 kinematic plane. This kinematic plot shows the deep inelastic regime and the resonance regime. The solid line corresponds to an invariant mass of the final state of $W = 2$ GeV. Every point above the line lies in the resonance region, $W < 2$ GeV, and every point below the line lies in the deep inelastic region $W > 2$ GeV. The invariant mass of the final state, W , is related to the four-momentum transfer Q^2 and Bjorken x_{Bj} by $W^2 = M^2 + Q^2[(1/x_{\text{Bj}}) - 1]$, where M is the nucleon mass.

[52]. They also extended only up to $x_{\text{Bj}} \approx 0.6$ [53–56]. This is due not only to the fact that polarization experiments are always more difficult to perform than unpolarized measurements, but mainly due to the fact that in order to achieve $x_{\text{Bj}} \rightarrow 1$ for the deep inelastic regime, one has to use very high four-momentum transfers Q^2 , see Fig. 1. This drastically reduces the cross section, as the cross section is proportional to the Mott cross section, which in turn is proportional to $1/Q^4$. Thus, accessing one and the same x_{Bj} in the resonance region and in the deep inelastic regime leads to much lower count rates in the deep inelastic regime. For example, a measurement at $x_{\text{Bj}} = 0.8$ can be performed at $Q^2 = 2$ GeV² in the resonance region, or at $Q^2 \geq 15$ GeV² in the deep inelastic region. The count rate in the deep inelastic region will be lowered by more than a factor of 50 compared to the resonance region measurement. This makes taking data in the deep inelastic regime for large x_{Bj} extremely difficult. A recent Jefferson Lab experiment improved the situation by measuring in the deep inelastic regime, up to $x_{\text{Bj}} \geq 0.6$ with very reasonable error bars, thus decreasing the uncertainty by an order of magnitude compared to older data [50,52]. Still, the experimental exploration of A_1^n at really large $x_{\text{Bj}} \rightarrow 1$ has not been feasible yet, thus making it the prime application for duality. Even with the planned 12 GeV upgrade of Jefferson Lab, data in the deep inelastic regime will be accessible only up to $x_{\text{Bj}} \approx 0.75$ [10].

As the kinematics plot shows, large values of x_{Bj} can be accessed at low Q^2 in the resonance regime. A measurement of A_1^n —or any other observable of interest—in the resonance region can then be averaged, and will yield the same information as a direct measurement in the deep inelastic region, provided that duality holds. Using this approach, A_1^n could be measured up to $x_{\text{Bj}} \approx 0.9$, by taking data in the Delta resonance region [57].

Another interesting application of duality that was recently discussed is the application of duality to the EMC effect [6]. Even though the EMC effect has been mapped out for a large kinematic region, data at very high x_{Bj} and for lighter nuclei are scarce. The data base could be significantly expanded by the application of duality to lepton scattering from nuclei.

Before we can embark on this new experimental approach, we need a good, solid understanding of how well duality holds, and where it holds. Ideally, one would come up with a certain accuracy of the duality procedure, which then could be quoted as a systematic error for the extraction of A_1^n or other observables in the relevant region. Here, we need more theoretical input and guidance. As we currently do not understand quark-hadron duality from first principles, modeling is our best tool to obtain the answers necessary for applying duality to extract A_1^n .

Currently, theorists tackle this problem by modeling duality in two different ways: one branch starts out from the nonrelativistic constituent quark model, with some

relativistic corrections, to describe duality [11,12,17–19], the other branch starts the modeling with a relativistic one-body equation [13,14,20–22,28–30]. The former branch makes contact with the phenomenology. It was started by the pioneering work of Close and Isgur [11], where the authors investigated how a summation over the appropriate sets of nucleon resonances leads to parton model results for the structure function ratios in the SU(6) symmetric quark model. This work was recently expanded [12] to include the effects of SU(6) spin-flavor symmetry breaking. In Refs. [17–19], the authors considered the first five low-lying resonances, and performed a careful analysis of the onset of duality for F_2 and g_1 . Our results belong to the latter branch. The goal of these modeling efforts is obvious: to gain an understanding of quark-hadron duality and the conditions under which it holds, by capturing just the essential physical conditions of this rather complex phenomenon. We imposed these basic requirements for a model: we require a relativistic description of confined valence quarks, and we treat the hadrons in the infinitely narrow resonance approximation.

This paper is the fourth in a series of papers, in which we have modeled duality with increasing complexity. All models that we have presented so far have reproduced the features of duality in a qualitative manner. We started out with an all scalar model [28], and gradually improved the model until all the particles had proper spin [30]. In Ref. [30], we focused on the model results for the unpolarized responses. For the first time, we investigated the dependence of our results on the type of potential we employed. In the present paper, we focus on the spin observables: the responses $R_{T'}$ and $R_{TL'}$ that are accessible only with spin, the spin structure functions g_1 and g_2 , and the polarization asymmetries A_1 and A_2 .

This paper is organized as follows: in Sec. II, we briefly state the properties of the model, then, in Sec. III, we discuss some of the formalism for polarized inclusive electron scattering. In Sec. IV we discuss our numerical results for the various spin observables for the bound-free and the bound-bound transitions. We end with a brief summary of our results and an outlook.

II. THE MODEL

We use the same model as in Ref. [30]. For the convenience of the reader, we present the key ingredients of our model here.

Our model consists of a constituent quark bound to an infinitely heavy diquark and is represented by the Dirac Hamiltonian

$$\hat{H} = \boldsymbol{\alpha} \cdot \hat{\mathbf{p}} + \beta[m + V_s(r)] + V_v(r), \quad (1)$$

where the scalar potential is a linear confining potential given by

$$V_s(r) = br, \quad b = 0.18 \text{ GeV}^2. \quad (2)$$

We have used the constituent quark mass in this paper, as our main interest is the study of quark-hadron duality, which sets in at rather low Q^2 , experimentally $Q^2 \approx 0.5 \text{ GeV}^2$ is enough. In this kinematic region, the appropriate degree of freedom is the constituent quark, which has acquired mass through spontaneous chiral symmetry breaking. We have used a value for the quark mass of $m = 258.46 \text{ MeV}$ —obtained previously in a fit to heavy mesons [58]. However, nothing hinges on using that particular value: we changed our quark mass to $m = 10 \text{ MeV}$, in order to have a value reminiscent of a current quark mass, and repeated our calculations. It turns out that, while scaling does set in a little faster, there are no qualitative changes in the results.

In our model, the vector potential is provided by a vector color Coulomb potential. Calculations will be presented where the vector color Coulomb potential is absent, that is $V_v(r) = 0$, where the vector potential is the simple static Coulomb potential

$$V_v(r) = V_c(r) = -\frac{4}{3} \frac{\alpha_s}{r} \quad (3)$$

with $\alpha_s = 0.181$ and where the color Coulomb potential is corrected to allow for the running coupling constant in a manner similar to that used by Godfrey and Isgur [59]. The vector potential then has the form

$$\begin{aligned} V_v(r) &= V_{cr}(r) \\ &= -\frac{4}{3r} \left[\alpha_c \frac{1 + e^{-\frac{\rho_0}{\delta}}}{1 + e^{(\sqrt{b}r - \rho_0)/\delta}} + \sum_{i=1}^2 \alpha_i \text{erf}(\gamma_i r) \right], \end{aligned} \quad (4)$$

where

$$\begin{aligned} \alpha_c &= 0.118, & \rho_0 &= 0.04, & \delta &= 0.01, \\ \alpha_1 &= 0.239, & \alpha_2 &= 0.271, & \gamma_1 &= 0.746 \text{ GeV}, \\ & & \gamma_2 &= 5.40 \text{ GeV}. \end{aligned} \quad (5)$$

Note that we use different scalar and vector potentials, in contrast to Refs. [21,22], where $V_s = V_v$ is used to simplify the calculations.

We assume that only the light quark carries a charge, and we choose unit charge for the light quark for simplicity.

III. SPIN OBSERVABLES

In this section, we briefly review the formalism for calculating responses for targets with arbitrary polarization axes, and connect the definitions of the polarization asymmetries A_1, A_2 and the spin structure functions g_1, g_2 to the responses.

The hadronic tensor for targets with an arbitrary polarization axis in \hat{s} direction is

$$W^{\mu\nu} = \sum_{m,m''} \omega_{mm''}^{\mu\nu} \left\langle \frac{1}{2} m'' \left| \frac{1}{2} (1 + \vec{\sigma} \cdot \hat{s}) \right| \frac{1}{2} m \right\rangle \quad (6)$$

with

$$\omega_{mm''}^{\mu\nu} = \sum_{n'l'j'm'} \left\langle 10\frac{1}{2}m \left| J^{\mu\dagger} |n'l'j'm'\rangle \langle n'l'j'm'| J^\nu \right| 10\frac{1}{2}m'' \right\rangle \quad (7)$$

where J is the electromagnetic current operator. The ground state's z component of j is denoted m instead of m_j for brevity. Components of the hadronic tensor can be combined to give

$$\begin{aligned} W_L &= W^{00}, & W_T &= W^{++} + W^{--}, \\ W_{TT} &= 2\Re(W^{+-}), & W_{TL} &= -2\Re(W^{0+} - W^{0-}), \\ W_{TL'} &= -2\Re(W^{0+} + W^{0-}), & W_{T'} &= W^{++} - W^{--}. \end{aligned} \quad (8)$$

The cross section for electron helicity h and target polarization axis \hat{s} can be expressed in terms of the hadronic tensor and the leptonic coefficients v_K , $K = L, T, TT, TL, T', TL'$ as

$$\frac{d\sigma}{dE'd\Omega'} = \sigma_M (v_L W_L + v_T W_T + v_{TL} W_{TL} + v_{TT} W_{TT} + h[v_{TL'} W_{TL'} + v_{T'} W_{T'}]) \quad (9)$$

where σ_{Mott} is the Mott cross section, \mathbf{q} is the three-momentum transfer from the electron to the target, ν is the energy transfer and $Q^2 = \mathbf{q}^2 - \nu^2$, and h denotes the electron helicity. The leptonic coefficients are given by [60]

$$v_L = \frac{Q^4}{q^4}, \quad v_T = \frac{Q^2}{2q^2} + \tan^2 \frac{\theta}{2}, \quad v_{T'} = \sqrt{\frac{Q^2}{q^2} + \tan^2 \frac{\theta}{2}} \tan \frac{\theta}{2}, \quad v_{TL'} = -\frac{1}{\sqrt{2}} \frac{Q^2}{q^2} \tan \frac{\theta}{2}. \quad (10)$$

For arbitrary target spin, all six combinations of the hadronic tensor are nonzero. However, for spin 1/2 targets, only four combinations contribute: L, T, TL' and T' . Inserting the results for the current matrix elements, and exploiting selection rules and symmetry relations between various current matrix elements, one finds for our case

$$\begin{aligned} W_L &= \frac{1}{2} \sum_m \sum_{n'l'j'} \left| \langle n'l'j'm | J^0 \left| 10\frac{1}{2}m \right\rangle \right|^2 [1 + s_z (-1)^{1/2-m}], \\ W_T &= \frac{1}{2} \sum_m \sum_{n'l'j'} [1 + s_z (-1)^{1/2-m}] \left[\left| \langle n'l'j'm + 1 | J^+ \left| 10\frac{1}{2}m \right\rangle \right|^2 + \left| \langle n'l'j'm - 1 | J^- \left| 10\frac{1}{2}m \right\rangle \right|^2 \right], \\ W_{T'} &= \frac{1}{2} \sum_m \sum_{n'l'j'} [1 + s_z (-1)^{1/2-m}] \left[\left| \langle n'l'j'm + 1 | J^+ \left| 10\frac{1}{2}m \right\rangle \right|^2 - \left| \langle n'l'j'm - 1 | J^- \left| 10\frac{1}{2}m \right\rangle \right|^2 \right], & W_{TT} &= 0, \\ W_{TL} &= 0, & W_{TL'} &= -2s_x \sum_{n'l'j'} \Re \left(\left\langle 10\frac{1}{2}\frac{1}{2} \left| J_0^\dagger \left| n'l'j'\frac{1}{2} \right\rangle \langle n'l'j'\frac{1}{2} \left| J^+ \left| 10\frac{1}{2}-\frac{1}{2} \right\rangle \right. \right. \right). \end{aligned} \quad (11)$$

Explicitly carrying out the summation over the initial spin m for the T' and TL' combinations, and substituting for the hadronic tensor combinations in the expression for the cross section Eq. (9), we find:

$$\begin{aligned} \frac{d\sigma}{dE'd\Omega'} &= \sigma_M \left[v_L \frac{1}{2} \sum_m \sum_{n'l'j'} |J^0(m)|^2 + v_T \frac{1}{2} \sum_m \sum_{n'l'j'} [|J^+(m)|^2 + |J^-(m)|^2] \right. \\ &\quad \left. + h \left[-2s_x v_{TL'} \sum_{n'l'j'} \Re \left[J^{0,\dagger} \left(\frac{1}{2} \right) J^+ \left(-\frac{1}{2} \right) \right] + v_{T'} s_z \sum_{n'l'j'} \left[\left| J^+ \left(\frac{1}{2} \right) \right|^2 - \left| J^- \left(-\frac{1}{2} \right) \right|^2 \right] \right] \right] \quad (12) \end{aligned}$$

where we abbreviated the current matrix elements as $J^\mu(m)$ for $\langle n'l'j'm | J^\mu | 10\frac{1}{2}m \rangle$. Now we can relate this cross section to the definition of the polarization observables. The polarization asymmetry A_{\parallel} is defined as the ratio of the difference and sum of the cross sections for longitudinally polarized electrons and target polarization parallel or antiparallel to the beam, see e.g. [61,62]:

$$A_{\parallel} = \left[\frac{d\sigma^-}{dE'd\Omega'} - \frac{d\sigma^+}{dE'd\Omega'} \right] / \left[\frac{d\sigma^-}{dE'd\Omega'} + \frac{d\sigma^+}{dE'd\Omega'} \right]. \quad (13)$$

The upper superscript denotes the direction of the electron polarization, the lower superscript indicates the direction of the target polarization. The relevant cross sections are obtained by using $h = 1$ in each case and \hat{s} and $-\hat{s}$ for the target polarizations parallel and antiparallel to the beam. Using the conventional coordinate system, this means that the target is polarized in the $x - z$ plane, see e.g. [61,62]. In this case, $\hat{s} = (\sin\alpha, 0, \cos\alpha)$, where α is the angle between transferred momentum \vec{q} and beam momentum \vec{k} : $\cos\alpha = (Q^2 + 2E_{\text{beam}}\nu)/2E_{\text{beam}}q$. Substituting and rearranging now yield:

$$A_{\parallel} = \frac{\nu_{T'} s_z}{\nu_T + \nu_L \frac{R_L}{R_T}} \left(\frac{-\sum_{n'l'j'} [|J^+(\frac{1}{2})|^2 - |J^-(-\frac{1}{2})|^2]}{R_T} + 2 \frac{s_x}{s_z} \frac{\nu_{TL'}}{\nu_{T'}} \frac{\sum_{n'l'j'} \Re[J^{0,\dagger}(\frac{1}{2})J^+(-\frac{1}{2})]}{R_T} \right). \quad (14)$$

Now, we compare this expression to the definition of the polarization asymmetries A_1, A_2 . For the convenience of the reader, we quote the standard definitions [61,62]:

$$A_{\parallel} = D(A_1 + \eta A_2) \quad (15)$$

with the depolarization factor D

$$D = \frac{1 - (1 - y)\epsilon}{1 + \epsilon R} \quad (16)$$

where $y = \nu/E_{\text{beam}}$ and $R = \sigma_L/\sigma_T = W_2/W_1[1 + (\nu^2/Q^2)] - 1$, and

$$\eta = \frac{\epsilon \gamma y}{1 - \epsilon(1 - y)} \quad (17)$$

with the magnitude of the virtual photon's longitudinal polarization, $\epsilon = [1 + 2(q^2/Q^2)\tan^2(\theta_e/2)]^{-1}$, and $\gamma = 2Mx_{Bj}/\sqrt{Q^2}$. Note that the y defined here is not the y variable used in the next section. Thus, we can read off the expressions for the polarization asymmetries in terms of response functions from Eq. (14) as

$$A_1 = -\frac{R_{T'}}{R_T}, \quad A_2 = -\frac{1}{\sqrt{2}} \frac{Q}{q} \frac{R_{TL'}}{R_T} \quad (18)$$

where we used the symmetry of the current matrix elements and the definitions for the responses [60]:

$$\begin{aligned} R_L &= \overline{\sum_{i,f}} |J^0|^2, & R_T &= \overline{\sum_{i,f}} (|J^+|^2 + |J^-|^2), \\ R_{T'} &= \overline{\sum_{i,f}} (|J^+|^2 - |J^-|^2), \\ R_{TL'} &= -2 \overline{\sum_{i,f}} \Re[J^{0,\dagger}(J^+ + J^-)]. \end{aligned} \quad (19)$$

The symbol $\overline{\sum_{i,f}}$ indicates the average over initial states and the sum over final states. The spin structure functions can be found as functions of the responses using the relation between polarization asymmetries and spin structure functions:

$$A_1 = \frac{g_1 - \gamma^2 g_2}{F_1}, \quad A_2 = \gamma \frac{g_1 + g_2}{F_1} \quad (20)$$

with the unpolarized structure function $F_1 = MW_1 = \frac{1}{2}MR_T$. We find:

$$\begin{aligned} g_1 &= -\frac{1}{2}M \frac{\nu^2}{q^2} \left(R_{T'} + \frac{1}{\sqrt{2}} \frac{Q^2}{q\nu} R_{TL'} \right), \\ g_2 &= \frac{1}{2}M \frac{\nu^2}{q^2} \left(R_{T'} - \frac{1}{\sqrt{2}} \frac{\nu}{q} R_{TL'} \right). \end{aligned} \quad (21)$$

Summarizing our expressions for the polarization observables in terms of response functions, we have

$$\begin{aligned} A_1 &= -\frac{R_{T'}}{R_T}, & A_2 &= -\frac{1}{\sqrt{2}} \frac{Q}{q} \frac{R_{TL'}}{R_T}, \\ g_1 &= -\frac{1}{2}M \frac{\nu^2}{q^2} \left(R_{T'} + \frac{1}{\sqrt{2}} \frac{Q^2}{q\nu} R_{TL'} \right), \\ g_2 &= \frac{1}{2}M \frac{\nu^2}{q^2} \left(R_{T'} - \frac{1}{\sqrt{2}} \frac{\nu}{q} R_{TL'} \right). \end{aligned} \quad (22)$$

For completeness, we also quote the expressions for the unpolarized structure functions W_1 and W_2 in terms of the responses:

$$W_1(Q^2, \nu) = \frac{1}{2}R_T(q, \nu) \quad (23)$$

and

$$W_2(Q^2, \nu) = \frac{Q^4}{q^4} R_L(q, \nu) + \frac{Q^2}{2q^2} R_T(q, \nu). \quad (24)$$

We focused on the longitudinal and transverse response functions in our last paper [30], and we now focus on the true spin observables, which we can now calculate, as quark spin is included in our present model.

The Dirac wave functions and energy eigenvalues are obtained by integrating the Dirac equation using the Runge-Kutta-Feldberg technique and solutions are obtained for energies up to 12 GeV with the radial quantum number of $n \cong 200$ and $|\kappa| \leq 70$.

In our model, we excite the bound quark from the ground state to higher energy states, and do not allow it to decay. We refer to this process as the bound-bound transition (previously, in Ref. [30], we referred to it as final state interaction). Thus, we do not include any particle production in our model, and are strictly quantum-mechanical in this sense. We do not have any gluons in our model, either, which means that we do not encounter any radiative corrections. Since the response functions consist of a sum of delta functions, we choose to smear out the response functions by folding with a narrow Gaussian for purposes of visualization. The smeared response functions are then given by

$$R_K(q, \nu) = \frac{1}{\sqrt{\pi}\epsilon} \int_{-\infty}^{\infty} d\nu' e^{-[(\nu-\nu')^2/\epsilon^2]} R_K^{\text{unsmeared}}(q, \nu'), \quad (25)$$

where K stands for L, T, T' or TL' .

Before presenting numerical results, we would like to remind our readers that, while the present model is more

realistic than its predecessors, its results should not be compared *quantitatively* to inclusive electron scattering from a nucleon. Because of the assumption of an infinitely heavy antiquark (or diquark) to which the light quark is bound, our calculation most resembles inclusive electron scattering from a B meson, which has never been measured. The goal of our work is to gain a qualitative understanding of duality, and the current simplification is no impediment to this.

As discussed in Ref. [30], the current matrix elements naturally are functions of the three-momentum transfer q . Therefore, it is convenient to show our results for fixed three-momentum transfer q as a function of the y -scaling variable

$$y = \sqrt{(\nu + E_0)^2 - m^2} - q. \quad (26)$$

The physics are not affected by presenting our results in this fashion. In fact, later on we will explicitly compare our results plotted for fixed q and y to our results plotted for fixed four-momentum transfer Q^2 and the appropriate x -scaling variable.

In the following, we will present analytic and numerical results for the bound-free and bound-bound transitions, and we investigate if duality holds or not. The conditions that need to be fulfilled to see duality are scaling of the bound-bound transition and bound-free transition to the same scaling curve, and oscillation of the bound-bound results at low momentum transfer around the scaling curve. We are going to check if our model results qualitatively reproduce the signature of duality as seen in the electron scattering data.

In each case, we will investigate the approach to scaling for the different observables, the scaling curves themselves, and the behavior at low momentum transfers.

IV. NUMERICAL RESULTS

Now, we turn to the numerical results of our model calculations. Within our model, we calculate two different processes: the bound-bound transition and the bound-free transition of the light quark. The bound-free transition (referred to as plane wave impulse approximation in Ref. [30]) is the analog to perturbative QCD. The bound quark is knocked into the continuum by the absorption of the virtual photon.

We discuss the bound-free transition first, employing just the linear confining potential. We investigate the scaling results and the onset of scaling for the bound-free transition. Next, in Sec. IV C, we show our results for the bound-bound transition and the linear confining potential. There, we focus on the onset of scaling and the low- q duality. Then, we take a look at the role of the ground-state p -wave contribution in Sec. IV D. Finally, we investigate the effect of employing a static Coulomb and a running Coulomb potential in Sec. IV E.

A. y scaling for the bound-free transition

For the bound-free transition, we can reach arbitrarily high energy transfers without any numerical complications, as we do not have to solve for any high energy bound states in the final state. Moreover, we can determine the analytic expressions for the responses, and thus for all other observables, for $q \rightarrow \infty$ at fixed y . As the responses R_L and R_T , which can be accessed in unpolarized scattering, enter some spin observables, we quote all four responses for the reader's convenience [30]:

$$R_L(q, y) = \frac{1}{16\pi^2 q} \int_{|y|}^{y+2q} dp p \left\{ \sqrt{(y+q)^2 + m^2} n_v^0(p) + mn_s(p) + \frac{y^2 + 2qy + p^2}{2p} n_v^s(p) \right\} \quad (27)$$

$$R_T(q, y) = \frac{1}{8\pi^2 q} \int_{|y|}^{y+2q} dp p \left\{ \sqrt{(y+q)^2 + m^2} n_v^0(p) - mn_s(p) - \frac{y^2 + 2qy + 2q^2 - p^2}{2q} \times \frac{y^2 + 2qy - p^2}{2pq} n_v^s(p) \right\}, \quad (28)$$

$$R_{T'}(q, y) = -\frac{1}{8\pi^2 q} \int_{|y|}^{y+2q} dp p \left\{ [\sqrt{(y+q)^2 + m^2} + m] n_-(p) - pn_v^s(p) \left(\frac{y^2 + 2yq - p^2}{2pq} \right)^2 + \sqrt{(y+q)^2 + m^2} n_s(p) - mn_v^0(p) - \frac{y^2 + 2yq - p^2}{2p} n_v^s(p) \right\}, \quad (29)$$

and

$$R_{TL'}(q, y) = \frac{\sqrt{2}}{8\pi^2 q} \int_{|y|}^{y+2q} dp p \left\{ \frac{q}{2} \left[1 - \left(\frac{y^2 + 2yq - p^2}{2pq} \right)^2 \right] \times n_-(p) + qn_s(p) - \frac{y^2 + 2yq - p^2}{2pq} [mn_v^s(p) - pn_s(p)] \right\}. \quad (30)$$

In the limit of large q , the bound-free response functions become

$$\lim_{q \rightarrow \infty} R_L(q, y) = \frac{1}{16\pi^2} \int_{|y|}^{\infty} dp p \left\{ n_v^0(p) + \frac{y}{p} n_v^s(p) \right\} \quad (31)$$

$$\lim_{q \rightarrow \infty} R_T(q, y) = \frac{1}{8\pi^2} \int_{|y|}^{\infty} dp p \left\{ n_v^0(p) - \frac{y}{p} n_v^s(p) \right\}, \quad (32)$$

$$\lim_{q \rightarrow \infty} R_{T'}(q, y) = -\frac{1}{8\pi^2} \int_{|y|}^{\infty} dp p \left\{ \frac{y^2}{p^2} n_-(p) + n_s(p) - \frac{y}{p} n_v^s(p) \right\}, \quad (33)$$

and

$$\lim_{q \rightarrow \infty} R_{TL'}(q, y) = \frac{\sqrt{2}}{8\pi^2} \int_{|y|}^{\infty} dp p \left\{ \left(1 - \frac{y^2}{p^2}\right) \frac{1}{2} n_-(p) + n_s(p) \right\}. \quad (34)$$

These response functions therefore scale in y .

The vector and scalar momentum density distributions $n_v(p)$ and $n_s(p)$ are defined in terms of the ground-state wave function

$$\Psi_{10\frac{1}{2}m}(\mathbf{p}) = \begin{pmatrix} \psi_{10\frac{1}{2}}^{(+)}(p) \mathcal{Y}_{0\frac{1}{2}}^m(\Omega_p) \\ \psi_{10\frac{1}{2}}^{(-)}(p) \mathcal{Y}_{1\frac{1}{2}}^m(\Omega_p) \end{pmatrix} \quad (35)$$

as

$$n_v(p) = \left[n_v^0(p), \frac{\mathbf{p}}{|\mathbf{p}|} n_v^s(p) \right] \quad (36)$$

with

$$n_v^0(p) = \frac{1}{2\pi} [\psi_{10\frac{1}{2}}^{(+)\prime 2}(p) + \psi_{10\frac{1}{2}}^{(-)\prime 2}(p)] \quad (37)$$

and

$$n_v^s(p) = \frac{1}{\pi} \psi_{10\frac{1}{2}}^{(+)}(p) \psi_{10\frac{1}{2}}^{(-)}(p); \quad (38)$$

and

$$n_s(p) = \frac{1}{2\pi} [\psi_{10\frac{1}{2}}^{(+)\prime 2}(p) - \psi_{10\frac{1}{2}}^{(-)\prime 2}(p)]; \quad (39)$$

moreover,

$$n_-(p) = \frac{1}{\pi} [\psi_{10\frac{1}{2}}^{(-)\prime 2}(p)]. \quad (40)$$

The asymptotic responses for the bound-free transition are shown in Fig. 2. The two purely transverse responses, R_T and $R_{T'}$, have opposite signs but similar peak positions at slightly negative y values and peak heights. The longitudinal response R_L is the smallest of the four responses, and the only one to peak at a slightly positive y . The transverse-longitudinal interference response is the largest response, and peaks at $y = 0$. This response is symmetric around $y = 0$ as it contains only terms proportional to y^0 and y^2 , but no contributions linear in y .

The similar size and shape of R_T and $R_{T'}$, together with their opposite signs, leads to a value of the polarization asymmetry $A_1 = -(R_{T'}/R_T)$ close to 1, see Fig. 3. We show A_1 only for y values for which the responses have appreciable values, i.e., for $-1 < y < 0.6$. While we could calculate A_1 in a region where the responses are tiny, the

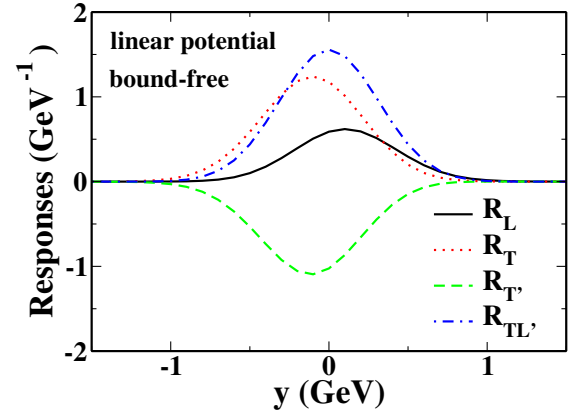


FIG. 2 (color online). The asymptotic behavior for $q \rightarrow \infty$ and fixed y of the responses for the bound-free transition. We show R_L (solid line), R_T (dotted line), $R_{T'}$ (dashed line), and $R_{TL'}$ (dashed-dotted line).

results would be meaningless. Our result is close to the pQCD prediction of 1 for A_1 in the limit of $x \rightarrow 1$. For large Q^2 , large negative values of y —much bigger than $y = -1$ GeV—correspond to $x = 1$.

The asymptotic values of the spin structure functions g_1 and g_2 are also shown in Fig. 3. The spin structure functions have peaks at small, negative y values. They have opposite signs. Of the two functions, g_2 has the slightly larger peak value. Note that the asymptotic value of A_2 is zero.

B. Approach to scaling in the bound-free transition

Now, after showing the asymptotic values, we will consider the approach to scaling in the bound-free transition. Previously, we have studied the approach to scaling of the unpolarized longitudinal and transverse response functions [30]. There, we found that the onset of scaling is not

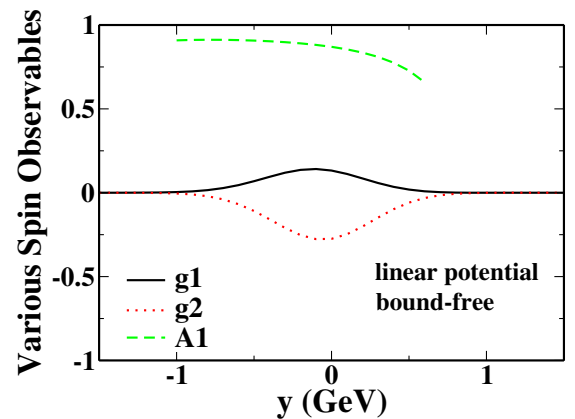


FIG. 3 (color online). The asymptotic behavior for $q \rightarrow \infty$ and fixed y of the spin structure functions g_1 and g_2 and the polarization asymmetry A_1 for the bound-free transition. We show g_1 (solid line), g_2 (dotted line), and A_1 (dashed line). Note that A_2 vanishes in this limit.

influenced very much by the spin of the target particle. The two response functions $R_{T'}$ and $R_{TL'}$ are accessible only with polarized beams and targets. It is interesting to check if they scale just like their unpolarized counterparts.

The scaling behavior of the transverse-primed response $R_{T'}$ for the bound-free transition is shown in Fig. 4. The lower panel shows the response for several q values up to 10 GeV. With increasing momentum transfer, the peak of the response moves to more negative values of y , and increases in height. The width of the response also increases. The change in the response when going from $q = 2$ GeV to $q = 4$ GeV is significant, and the difference between the $q = 4$ GeV and $q = 6$ GeV results is noticeable. Increasing q leads to very small changes, visible mainly at the peak and the large, negative y flank. The top panel, displaying the response for various higher values of q and the asymptotic value discussed above, shows that the response has converged to the asymptotic value roughly at $q = 40$ GeV.

The transverse-longitudinal primed response $R_{TL'}$ for the bound-free transition is shown in Fig. 5. The figure

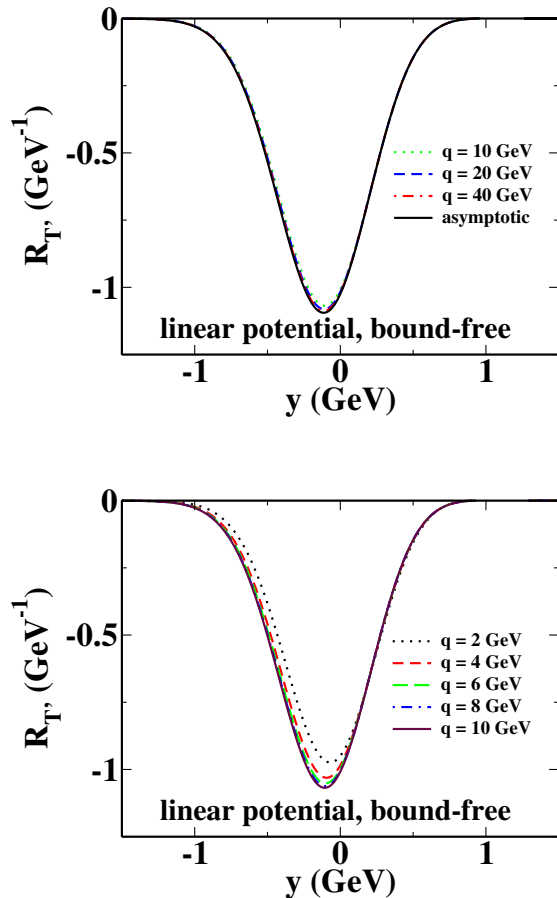


FIG. 4 (color online). The transverse-primed response function $R_{T'}$ is plotted versus y for several low (bottom panel) and high (top panel) values of the three-momentum transfer q . The results shown have been calculated for the bound-free transition, using the linear potential.

shows the response for lower values of the three-momentum transfer q . While there are small changes, amounting to a small shift of the entire response towards the negative y values, one can see that this response scales much faster than $R_{T'}$. We do not include another panel with $R_{TL'}$ calculated for higher q values, as the curves all coincide.

From this, we can see that the transverse-primed response $R_{T'}$ shows a scaling behavior very similar to R_T (as discussed in Ref. [30]), and that the only interference response that is accessible in inclusive electron scattering, $R_{TL'}$, exhibits the earliest onset of scaling.

Now, we will consider the y -scaling behavior of the spin structure functions. The spin structure functions are simply combinations of the spin-dependent responses multiplied with some kinematic factors, see Sec. III. We have already seen how the relevant responses, $R_{T'}$ and $R_{TL'}$, scale. Taking a look at the kinematic coefficients shows us that the onset of y scaling will be determined by the q values at which the kinematic factors reach their asymptotic values. For the convenience of the reader, we recall Eq. (22) here:

$$\begin{aligned} g_1 &= -\frac{1}{2}M\frac{\nu^2}{q^2}\left(R_{T'} + \frac{1}{\sqrt{2}}\frac{Q^2}{q\nu}R_{TL'}\right) \\ &= -\frac{1}{2}M\frac{\nu^2}{q^2}R_{T'} - \frac{1}{2\sqrt{2}}M\frac{\nu Q^2}{q^3}R_{TL'} \\ g_2 &= \frac{1}{2}M\frac{\nu^2}{q^2}\left(R_{T'} - \frac{1}{\sqrt{2}}\frac{\nu}{q}R_{TL'}\right) \\ &= \frac{1}{2}M\frac{\nu^2}{q^2}R_{T'} - \frac{1}{2\sqrt{2}}M\frac{\nu^3}{q^3}R_{TL'}. \end{aligned}$$

The asymptotic values of the kinematic factors multiplying the responses are, for fixed y and large q ,

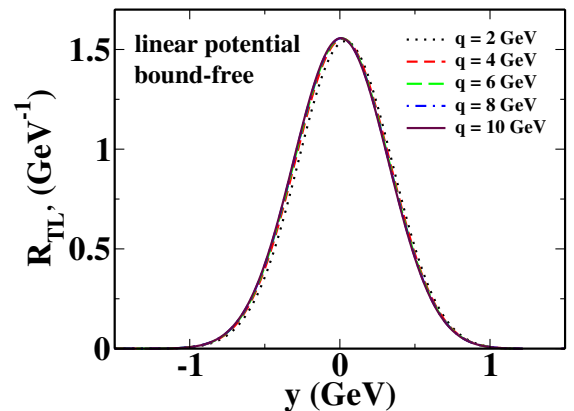


FIG. 5 (color online). The transverse-primed response function $R_{TL'}$ is plotted versus y for several values of the three-momentum transfer q . The results shown have been calculated for the bound-free transition, using the linear potential.

$$\begin{aligned} \frac{\nu^2}{q^2} &\rightarrow 1 + \frac{1}{q} 2(y - E_0) \rightarrow 1, \\ \frac{\nu Q^2}{q^3} &\rightarrow \frac{1}{q} 2(E_0 - y) \rightarrow 0, \quad \frac{\nu^3}{q^3} \rightarrow 1 + \frac{1}{q} 3(y - E_0) \rightarrow 1 \end{aligned} \quad (41)$$

leading to the asymptotic values of the spin structure functions:

$$g_1 \rightarrow -\frac{1}{2} M R_{T'}, \quad g_2 \rightarrow \frac{1}{2} M \left(R_{T'} - \frac{1}{\sqrt{2}} R_{TL'} \right). \quad (42)$$

From Eq. (41), one can see that the relevant scale for the onset of scaling is given by the ground-state energy E_0 . All responses peak roughly in the region $y \approx 0$, so that the three-momenta q necessary to reach the asymptotic values are determined by E_0 alone. The spin structure function g_1 for the bound-free transition is shown in Fig. 6. The lower

panel shows the spin structure function for several q values up to 10 GeV. One can see clearly that g_1 changes significantly for each increase in q , and that convergence has not set in at $q = 10$ GeV. This behavior is due to the slow approach of the kinematic factors in g_1 to their asymptotic values. The responses themselves scale much faster, and are very close to their asymptotic values at $q = 10$ GeV, whereas the spin structure function g_1 is off its asymptotic value by almost 50%. Results for g_2 at lower (bottom panel) and higher (top panel) three-momentum transfers are shown in Fig. 7. Just like g_2 , it approaches its scaling limits only at high momentum transfers.

The polarization asymmetries A_1 and A_2 are ratios of response functions, and may therefore show a different scaling behavior than the responses themselves. As we have seen that the two purely transverse responses, R_T and $R_{T'}$, have a very similar approach to scaling, one may expect to see an even more rapid scaling of A_1 , the ratio of the two transverse responses. The results for A_1 are shown in the top panel of Fig. 8. As A_1 is a pure ratio of two

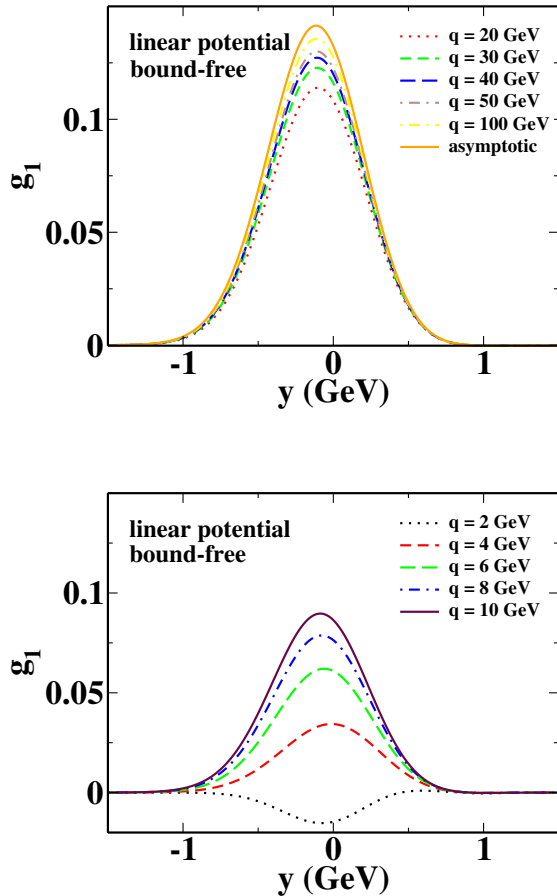


FIG. 6 (color online). The spin structure function g_1 is plotted versus y for several low (bottom panel) and high (top panel) values of the three-momentum transfer q . The results shown have been calculated for the bound-free transition, using the linear potential.

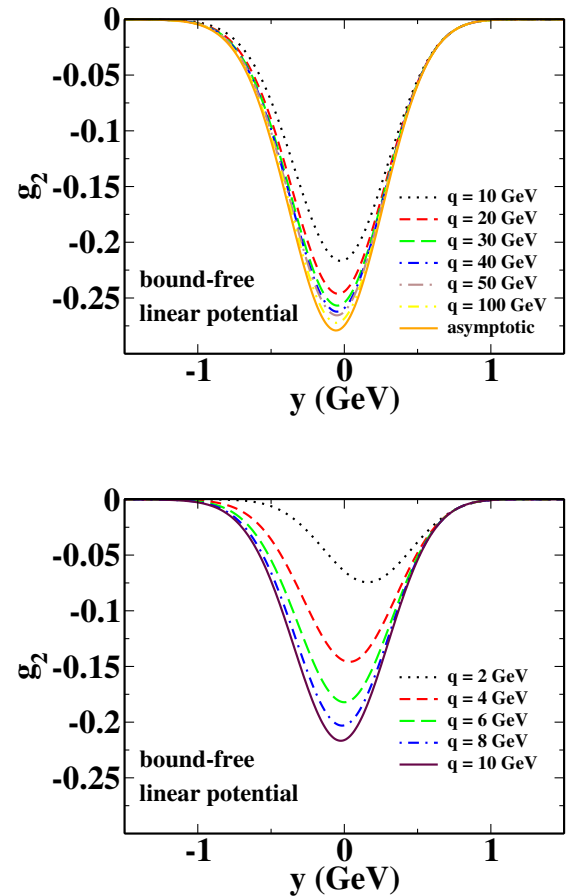


FIG. 7 (color online). The spin structure function g_2 is plotted versus y for several low (bottom panel) and high (top panel) values of the three-momentum transfer q . The results shown have been calculated for the bound-free transition, using the linear potential.

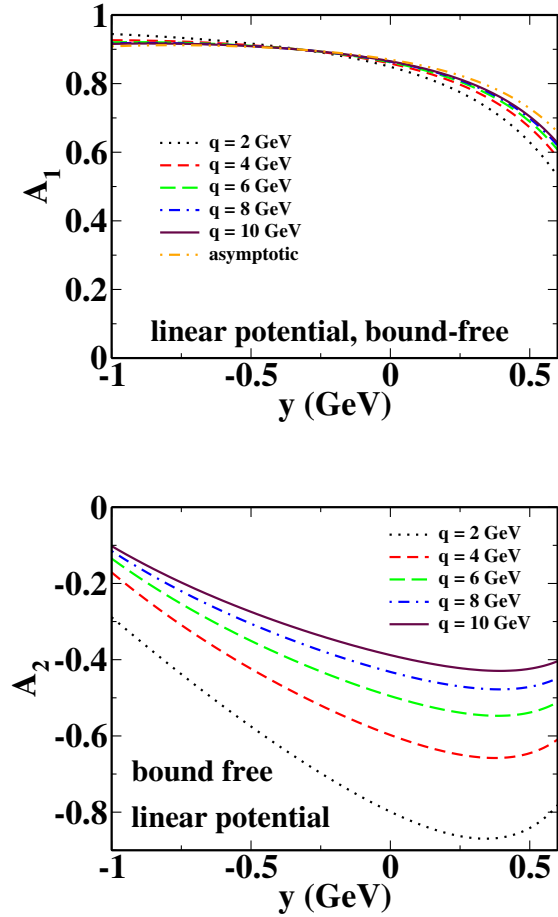


FIG. 8 (color online). The polarization asymmetries A_1 (top panel) and A_2 (bottom panel) are plotted versus y for several values of the three-momentum transfer q , as well as their asymptotic value for $q \rightarrow \infty$. The results shown have been calculated for the bound-free transition, using the linear potential.

responses that scale at reasonable values of q , without any kinematic factors, we can expect A_1 to scale fast. Indeed, one clearly sees that in the region of $-0.5 < y < 0$, where the responses are largest, A_1 scales almost immediately. Only the $q = 2$ GeV curve differs very slightly from all the other curves, including the asymptotic value, in this y interval. Outside of that region, where the responses have less strength, the scaling takes a bit longer. In all cases, $q = 10$ GeV is very close to the asymptotic value.

The approach to scaling of the polarization asymmetry A_2 is shown in the bottom panel of Fig. 8. Note that $A_2 \rightarrow 0$ for $q \rightarrow \infty$ and fixed y , because the kinematic factor $\frac{2}{q}$ goes to zero in this limit and the responses scale in y . Thus, the approach to scaling of A_2 will mainly be determined by the kinematic factor $\frac{Q}{q}$. So, even though both R_{TL} and R_T scale at reasonable values of q , the scaling of A_2 is delayed. The differences between the curves for increasing q values decrease, but the result for $q = 10$ GeV is still far away from the asymptotic value of 0. Just as for the spin structure

functions, the kinematic factor that is present determines the very slow onset of scaling.

In summary, we observe that the response functions reach values very close to their asymptotic values around $q = 10$ GeV, and scale at the latest at $q = 40$ GeV. The response R_{TL} is the fastest scaling response, and the response R_T is the response that scales most slowly. The spin structure functions and the polarization asymmetry A_2 scale only for much higher momentum transfers, due to the kinematic factors in their definitions. The polarization asymmetry A_1 , on the other hand, is the observable for which we observe scaling at the lowest momentum transfers.

Note that the scaling behavior of the discussed observables does not change when we use an “ x -type” scaling variable, as in our previous papers [28,29]. This is demonstrated in Fig. 9, where we show g_1 as a function of $u = \frac{1}{2m}(\sqrt{\nu^2 + Q^2} - \nu)[1 + \sqrt{1 + (4m^2/Q^2)}]$, for fixed Q^2 . Note that u goes to $u_\infty = (M_{\text{target}}/m)x_{\text{Bj}}$ for large Q^2 , its properties have been discussed previously [28,29]. This is the appropriate scaling variable for use with fixed Q^2 even at low Q^2 .

We have generated the plot by starting out with our results as functions of q and y , then calculated the corresponding values of the four-momentum transfer Q^2 and the scaling variable u . The results were then sorted into Q^2 bins. This is why there are no continuous lines in the figure, just single data points.

One can see clearly that the scaling behavior of g_1 is independent of the variables chosen: just as seen in Fig. 6 for fixed q and the variable y , at low Q^2 , g_1 starts out negative, then changes sign, and takes a very long time to scale. Even between the points for $Q^2 = 16$ GeV² and $Q^2 = 20$ GeV², there is a significant difference. Thus, we see that u scaling is just as slow for g_1 (and g_2 and A_2) as y scaling. The scaling behavior does not change at all with the use of different scaling variables.

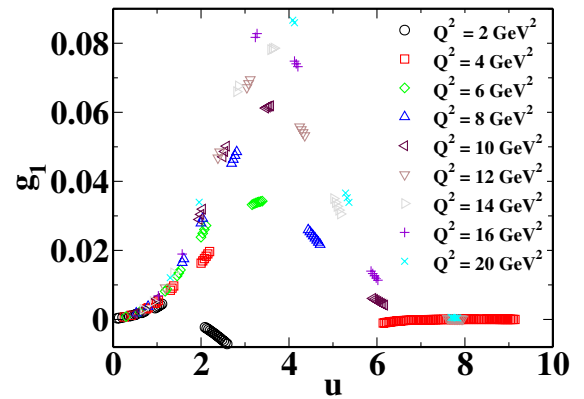


FIG. 9 (color online). The spin structure function g_1 is plotted versus u for several values of the four-momentum transfer squared Q^2 . The results shown have been calculated for the bound-free transition, using the linear potential.

C. Scaling and low q duality in the bound-bound transition

Now we proceed to discuss the behavior of the responses, spin structure functions, and polarization asymmetries for final states consisting solely of resonances. We refer to this case as the “bound-bound” transition. The wave functions for the excited states have to be obtained by solving the Dirac equation numerically. Because of the involved nature of the numerics, the highest accessible momentum transfer is $q = 10$ GeV. Work on extending our calculations up to 30 GeV using a WKB approximation will be reported elsewhere. Here, we focus on the approach to scaling and on duality at low q .

We start again by considering the two polarized responses. We show $R_{T'}$ in the top panel of Fig. 10. The resonance bumps at lower q values give way to smooth curves formed by many, closely spaced resonances. The graph shows that there is still a small difference between the results for $q = 8$ GeV and $q = 10$ GeV, we have not yet reached the scaling value. This is to be expected, as the

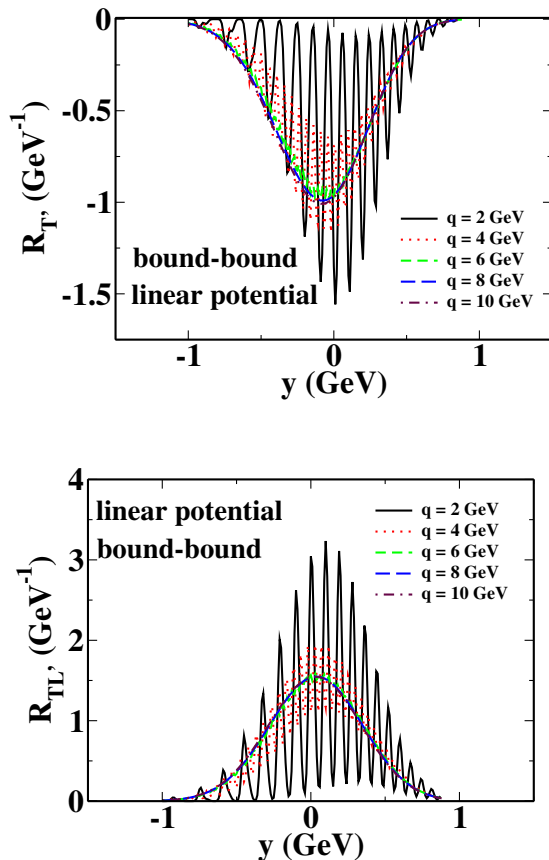


FIG. 10 (color online). The transverse-primed response function $R_{T'}$ (top panel) and the transverse-longitudinal primed response function $R_{T'L'}$ (bottom panel) are plotted versus y for several values of the three-momentum transfer q . The results shown have been calculated for the bound-bound transition, using the linear potential.

bound-free transition scales only at higher q values for this response. In general, the more complicated interplay of the various final state resonances leads to slower scaling for the bound-bound transition. The resonances oscillate around the smooth curves for higher momenta q on the positive y flank, but are a bit below the smooth curves at the negative y flank. We see a very similar behavior for $R_{TL'}$, in the bottom panel of Fig. 10.

For A_1 , the bound-bound transition results, shown in Fig. 11 scale very quickly in the region of the response peaks, $-0.5 < y < 0$. This is consistent with the scaling behavior of A_1 as observed in the bound-free transition, and stems from the definition of A_1 as ratio of two fast-scaling responses. It is interesting to note that the resonance bumps that are visible at $q = 2$ GeV have vanished almost completely at $q = 4$ GeV, even though they are clearly present at $q = 4$ GeV for the transverse and transverse-primed responses, whose ratio forms A_1 . This exemplifies the very quick onset of scaling for this observable, which we can observe even in the region of low momentum transfer q .

Our current model gives at best a very qualitative insight on the workings of duality for proton targets, as it is most closely related to electron scattering off a heavy-light meson, i.e., a B meson. Nevertheless, our results seem to be very encouraging as far as the prospects of applying quark-hadron duality to extracting deep inelastic information on A_1 from data in the resonance region are concerned.

The polarization asymmetry A_2 , which contains a kinematic factor multiplying the ratio of two responses, is shown in Fig. 12. In contrast to A_1 , A_2 changes significantly with changing momentum transfer, and approaches its scaling value of zero only slowly. As mentioned when discussing the bound-free transition results for A_2 in the previous section, the behavior of this polarization asymmetry is mainly determined by the kinematic factor, not by the ratio of the responses.

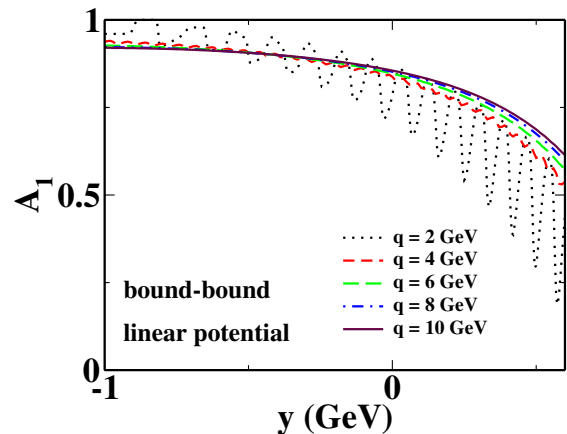


FIG. 11 (color online). The polarization asymmetry A_1 is plotted versus y for several values of the three-momentum transfer q . The results shown have been calculated for the bound-bound transition, using the linear potential.

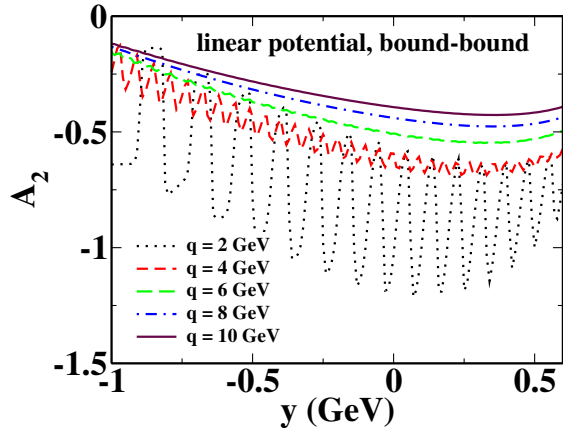


FIG. 12 (color online). The polarization asymmetry A_2 is plotted versus y for several values of the three-momentum transfer q . The results shown have been calculated for the bound-bound transition, using the linear potential.

The same scenario—large variation for changes in momentum transfer q and slow approach to the scaling values—is repeated for the spin structure functions g_1 and g_2 ,

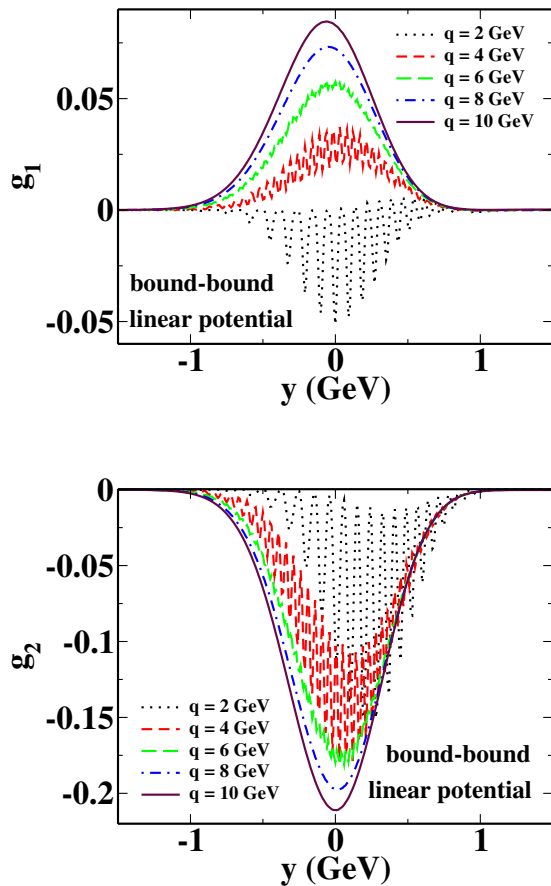


FIG. 13 (color online). The spin structure functions g_1 (top panel) and g_2 (bottom panel) are plotted versus y for several values of the three-momentum transfer q . The results shown have been calculated for the bound-bound transition, using the linear potential.

shown in Fig. 13. As for A_2 , their behavior is determined by the slowly scaling kinematic factors, not by the fast-scaling responses. For the lowest considered momentum transfer, g_1 even has a different sign, compared to the higher momentum transfer results.

Even though the onset of scaling is slow for A_2 , g_1 , and g_2 , one still observes that the bound-free results calculated for a specific momentum transfer q are dual to the bound-bound results for the same momentum transfer. This behavior can be seen in all observables, and we present the polarization asymmetries and spin structure functions in Figs. 14 and 15 calculated for the bound-bound and bound-free transitions at three-momentum transfers: $q = 2, 6, 10$ GeV. In Fig. 14, one can see that the bound-free result tracks the average bound-bound result very closely for the polarization asymmetries. Only for the lowest q value, $q = 2$ GeV, does the bound-free curve lie a bit above the average of the bound-bound curve at high y , and slightly below the bound-bound average at low y . The same behavior is observed for the spin structure functions

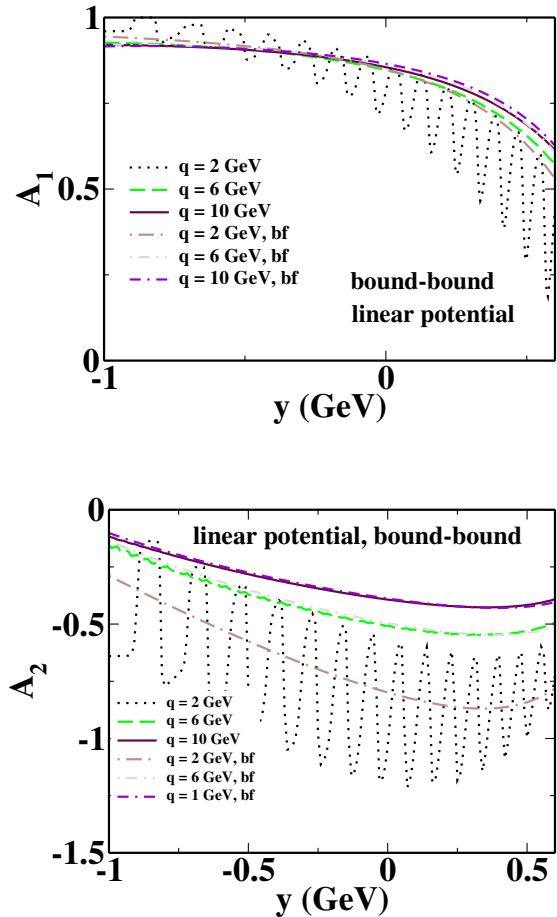


FIG. 14 (color online). A comparison of the bound-bound and bound-free results for the polarization asymmetries A_1 (top panel) and A_2 (bottom panel), plotted versus y for three values of the three-momentum transfer q . The results shown have been calculated using the linear potential.

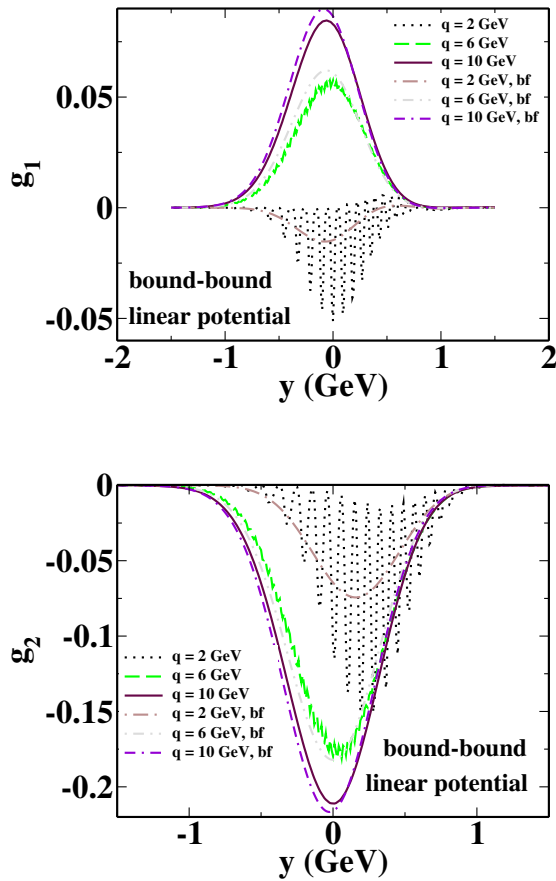


FIG. 15 (color online). A comparison of the bound-bound and bound-free results for the spin structure functions g_1 (top panel) and g_2 (bottom panel), plotted versus y for three values of the three-momentum transfer q . The results shown have been calculated using the linear potential.

plotted in Fig. 15. There, it is interesting to note that while the bound-free and bound-bound results agree almost perfectly in the positive y flank, for the peak region and the negative y flank, the bound-free results appear slightly larger.

Our results suggest that the application of duality to resonance region data for A_1 should be quite safe, while A_2 , g_1 , and g_2 seem to be observables that are less amenable to such an extraction procedure due to their very slow scaling.

As far as duality in the spin structure function g_1 is concerned, the available data [8,55,63,64] are not yet conclusive, and may imply a different onset of duality for g_1^p and g_1^n . The Hermes data [8] for g_1^p indicate that the onset of duality takes place at $Q^2 \approx 1.8 \text{ GeV}^2$. A recent analysis [5] of Jefferson Lab data [64] for the first moment of g_1^n indicates that duality could hold at Q^2 as low as 1 GeV^2 . A dedicated Jefferson Lab experiment to study duality in neutron spin structure functions in the resonance region is currently being analyzed [9]. Dong *et al.* [17–19] recently used a constituent quark model for the five lowest-

lying resonances and various parametrizations of scaling data for a careful theoretical analysis of duality in F_2 and g_1 for the proton target. They included target mass corrections and find that duality in g_1 is not seen below $Q^2 \approx 2 \text{ GeV}^2$. Close and Isgur [11], using an SU(6)-symmetric, constituent quark model, also predicted a slower onset of duality for g_1 , and pointed out that duality sets in faster in this model for g_1^n than for g_1^p . Dominant magnetic interactions are necessary for the symmetric quark model, and for the neutron target, this is realized.

Our simple model is, of course, far from describing actual electron scattering measurements. It is not intended to provide a quantitative description of data, but to provide qualitative insights into nature. However, our findings on the scaling behavior of the polarization asymmetries and spin structure function might provide more general guidance: what we see is that the onset of scaling is driven mainly by the kinematic factors multiplying the reasonably fast-scaling response functions in the definitions Eq. (22) of the spin structure functions and polarization asymmetries. Where the factors are missing, i.e., for A_1 , convergence is rapid and the prospects for a successful application of duality are very good. Where the factors are present, and take a very high momentum to reach their asymptotic value, e.g., in g_1 , scaling is very slow and duality does not hold. This suggests that the validity of quark-hadron duality in spin observables may be strongly related to kinematic factors, and less to dynamics. The faster scaling for g_1^n might be explained due to a smaller longitudinal-transverse interference response R_{TL} , see Eqs. (41) and (42).

However, one has to be cautious as certain features of nature are not included in our model: it is well known that the Δ resonance has an unnaturally small coefficient multiplying the leading term and therefore gives rise to peculiarities in the scaling and duality behavior, see [16].

D. The role of the p -wave contribution

One interesting question is which role the p wave in the ground state plays. We will discuss the role of the ground-state p -wave contribution for the onset of scaling for the observables, and for the scaling results themselves.

1. The p wave for the bound-free transition

For the bound-free transition, we can read off from the momentum distributions in Sec. IVA that, without the ground-state p wave,

$$n_v^0(p) = n_s(p) = \frac{1}{2\pi} \psi_{10\frac{1}{2}}^{(+)\prime 2}(p) \quad \text{and} \quad n_v^s(p) = n_-(p) = 0. \quad (43)$$

Thus, in the scaling limit, we can introduce the response

$$R_{nop} = \frac{1}{16\pi^3} \int_{|y|}^{\infty} dp p \psi_{10\frac{1}{2}}^{(+)\prime 2}(p) \quad (44)$$

and then write all the bound-free responses in the scaling limit as

$$R_L = \frac{1}{2}R_{nop}, \quad R_T = -R_{T'} = R_{nop}, \quad (45)$$

$$R_{TL'} = \sqrt{2}R_{nop}.$$

From these equations, one sees that in the scaling limit, the peak position is now identical for all four responses, and that the responses differ only by a simple numerical factor. This leads automatically to $A_1 = 1$ for all values of q and y . Just like the responses, the spin structure functions g_1 and g_2 also peak at $y = 0$ GeV without the p wave in the ground state. Apart from slight shifts in the peak position, there are no major changes in the asymptotic forms of the observables, see Fig. 16. For R_L , omission of the p wave

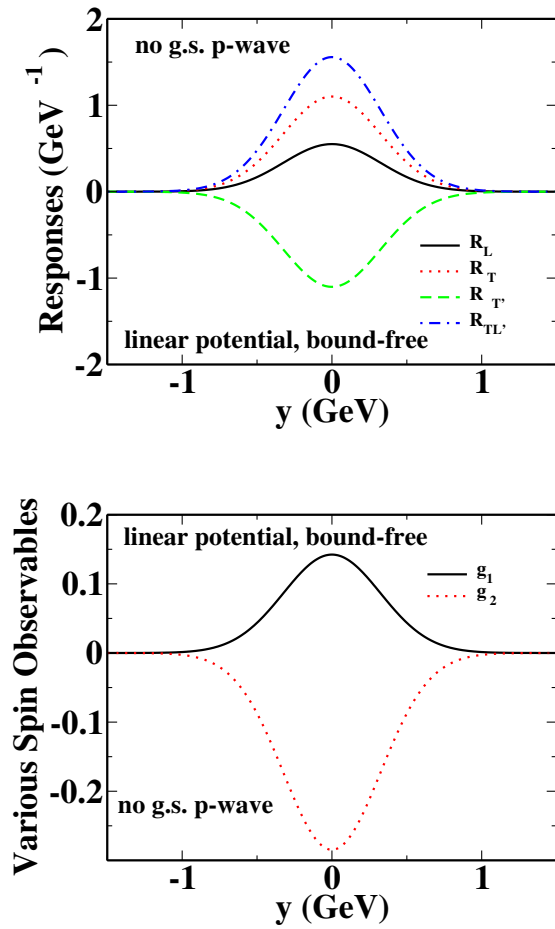


FIG. 16 (color online). The asymptotic behavior for $q \rightarrow \infty$ and fixed y of the responses for the bound-free transition, without the ground-state p wave (top panel). We show R_L (solid line), R_T (dotted line), $R_{T'}$ (dashed line), and $R_{TL'}$ (dashed-dotted line). The asymptotic behavior for $q \rightarrow \infty$ and fixed y of the spin structure functions g_1 and g_2 for the bound-free transition, without the ground-state p wave (bottom panel). We show g_1 (solid line) and g_2 (dotted line). Note that A_2 vanishes in this limit, and that $A_1 = 1$.

leads to a slight reduction in peak height. R_T also has a reduced peak height (a reduction of about 10%). In contrast, $R_{T'}$ maintains its peak height. The only response not to experience any noticeable change is $R_{TL'}$, which was centered around $y = 0$ GeV to start with, and does not change its peak height, either.

The omission of the p wave in the ground state simplifies the analytic expressions obtained for the responses, and one expects that scaling should set in more quickly. This is observed at low q values for R_L and R_T . For $R_{T'}$ and $R_{TL'}$, the presence of the p -wave contribution plays a negligible role in the scaling behavior. This behavior is consistent with the fact that the asymptotic forms of R_L and R_T are more strongly affected by the omission of the p wave.

For g_1 , the results change significantly for low q , see the top panel of Fig. 17. At $q = 2$ GeV, the spin structure function is changing sign at $y \approx 0.1$ GeV and becomes positive. For higher q values, g_1 peaks at slightly higher y values without p wave, and the peak height is somewhat

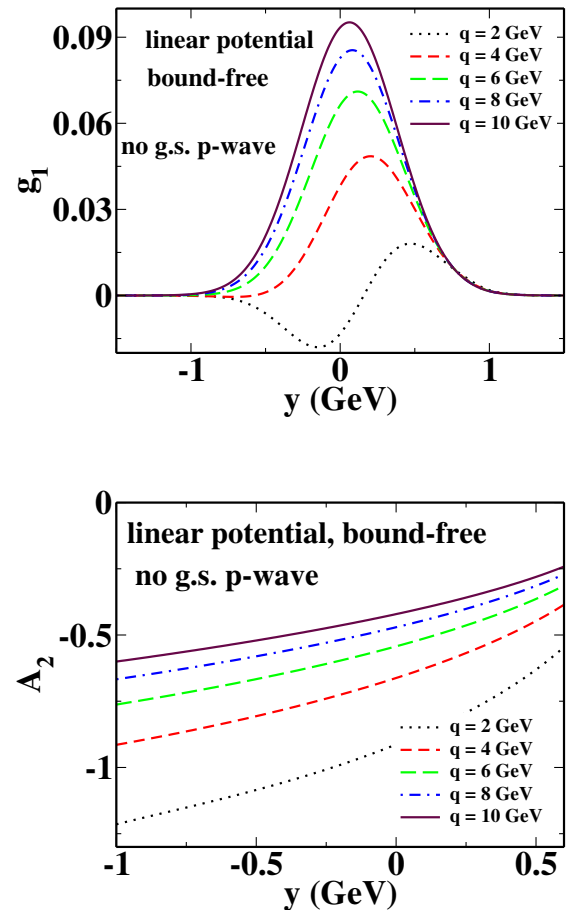


FIG. 17 (color online). The spin structure function g_1 (top panel) and the polarization asymmetry A_2 (bottom panel) are shown without the ground-state p wave for several values of the three-momentum transfer q at fixed y .

higher, too. The onset of scaling is very slow, independent of the p -wave contribution.

The onset of scaling is dramatically accelerated for A_1 by dropping the p wave, as R_T and R'_T coincide apart from an overall sign, and A_1 is the ratio of these two responses. Therefore, A_1 scales directly to 1 for even the lowest value of q , if there is no p wave present.

While A_2 is still scaling slowly, it has quite a different shape now, see the bottom panel of Fig. 17. Instead of starting at its maximum value at large negative y , and decreasing to a minimum around $y \approx 0.4$ GeV, without the p wave, it starts out at its minimum value at large negative y and steadily increases.

2. The p wave for the bound-bound transition

The situation for the bound-bound transition is similar: for the longitudinal response, we observe small changes in peak position and peak height due to the omission of the p wave, just like for the bound-free transition. For the transverse response, we see a more pronounced reduction in peak height, as well as the already familiar shift in the peak position. The transverse-longitudinal primed response remains largely unaffected by the omission of the p wave, while the transverse-primed response has a shifted peak position, and no reduction in peak height. These observations are very similar to the observations made above concerning the effects of the p wave on the asymptotic shapes of the responses for the bound-free transition.

The polarization asymmetry A_1 again takes the value of 1 immediately, as R_T and R'_T only differ by a sign. A_2 without the ground-state p wave has the same shape for bound-bound and bound-free transitions, markedly different from the shape including the p wave. The spin structure function g_1 behaves similarly for bound-bound and bound-free transitions, too. We do not present any figures for the bound-bound results, as they are so similar to the bound-free transition results shown above.

Strictly speaking, one would have to renormalize the remaining wave function when switching off the p wave. However, the effect of this rescaling will be small, and we omit it here. The goal of this discussion was to learn where the p wave is important, and where not. Summarizing, the p wave has the biggest impact on the polarization asymmetries, where switching off the p wave leads to immediate scaling for A_1 and a different shape for A_2 , before A_2 reaches its asymptotic value of zero. The spin structure function g_1 also shows sensitivity to the p -wave contribution at low q .

Our results for the role of the p wave in A_1 confirm the results in Ref. [22]. There, the authors noted a distinct suppression of A_1 at low Nachtmann ξ due to the p waves. The region of large positive y , where we observe a falloff of A_1 when it is calculated with the complete wave function, and find a value of 1 when A_1 is calculated without the p -wave contribution, corresponds to the low ξ region.

E. Model dependence

In this section, we discuss the influence of the chosen potential on the results for the observables. In all discussed cases, we use a scalar linear confining potential. In addition, we either use no vector potential, a static Coulomb potential, or a running Coulomb potential as vector potential, see Sec. II. For brevity, we restrict ourselves to the bound-bound transition. Previously [30], we found that there is no qualitative difference between the linear, linear plus static Coulomb, and linear plus running Coulomb results in the longitudinal and transverse responses. Peak height and position are different, but the approach to scaling and the low q oscillatory behavior are qualitatively the same.

First, we discuss the results for the linear plus static Coulomb potential in the bound-bound transition. The responses agree qualitatively with the results for just the linear potential, with similar shapes, peak heights, peak

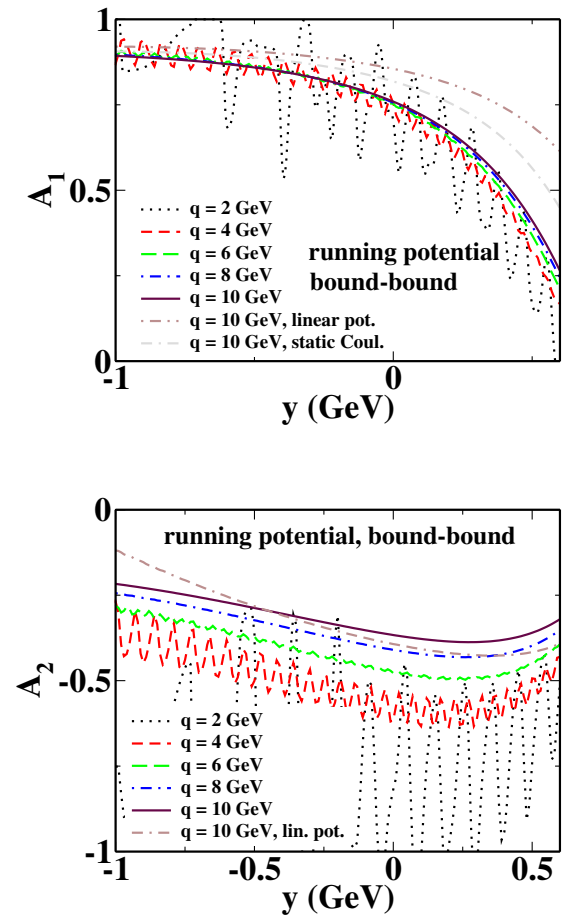


FIG. 18 (color online). The polarization asymmetries A_1 (top panel) and A_2 (bottom panel) are plotted versus y for several values of the three-momentum transfer q . The results shown have been calculated for the bound-bound transition, using the running Coulomb potential. The results for $q = 10$ GeV for the linear potential and the static Coulomb potential are also shown for comparison.

locations, and scaling behavior. The same holds for the spin structure functions g_1 and g_2 . For the polarization asymmetry A_1 , the decrease from values close to 1 is slightly more pronounced for positive y values, but the differences are still small.

This somewhat faster falloff of A_1 is seen more distinctly for the linear plus running Coulomb potential, see Fig. 18. However, the responses and spin structure functions look very similar for the linear plus running Coulomb potential and the linear plus static Coulomb potential. A_2 has a slightly different shape for the linear plus running Coulomb potential, it starts out more flatly at negative y values than for the linear potential and the linear plus static Coulomb potential. The onset of convergence, however, does not seem to be affected noticeably by the potential in the low q region.

These results for the dependence of the spin observables on the employed model potential are consistent with the results found for the behavior of the longitudinal and transverse response functions: while the results differ quantitatively, there is no qualitative difference due to the different potentials, neither in the results for the highest q valuable attainable for bound-bound transitions in our model, nor in the convergence of the results.

The polarization asymmetries, as ratios of responses, are naturally more sensitive than the other observables, but even they only show a minor influence of the potential.

V. SUMMARY AND OUTLOOK

We have presented results for responses, spin structure functions and polarization asymmetries, calculated within a simple model consisting of a light quark bound to an infinitely heavy antiquark (or a diquark) without charge. We have investigated the onset of scaling and the scaling functions themselves in the bound-free transition, where we are not hampered by the numerical difficulties involved in calculating the bound-bound transition for energies larger than 12 GeV. For the bound-bound transition, we looked at the approach to scaling and the duality at low momentum transfer q .

We have found that the two polarization responses, $R_{T'}$ and $R_{TL'}$, scale roughly like their unpolarized counterparts, the longitudinal and transverse responses R_L and R_T . The only interference response, $R_{TL'}$, scales a bit faster than the other responses, but the differences in scaling behavior are small. Duality holds qualitatively for the responses, and for the polarization asymmetry A_1 . In fact, A_1 scales rapidly, and judging from our model calculations, is the most promising observable for the application of duality to

extract deep inelastic scattering information from resonance region data. These results are reminiscent of the observation that the A_1^p and A_1^n data show little Q^2 dependence [65].

In contrast, scaling sets in very slowly for A_2 and the spin structure functions g_1 and g_2 . This behavior is independent of the type of scaling variable chosen: convergence for an x -type scaling variable and large Q^2 is as slow as for the y -scaling variable and increasing q . We have traced the reason for the slow onset of scaling back to the kinematic factors multiplying the responses in the expressions for the spin observables.

Of course, these are results calculated within a simple model, and the model should not be viewed as an attempt at a quantitative description of electron scattering off a proton. In nature, it may turn out that the scaling behavior of the responses is different, and might compensate in some way for the slow scaling of the kinematic factors. Still, our model calculations might provide some useful guidance. It would be interesting to investigate if the responses can be separated from the data available at present, and to see if they indeed scale and exhibit duality as predicted in our model.

As in Ref. [30], we have performed calculations for three different potentials. The quantitative differences are small for almost all observables, and qualitatively, a different potential does not seem to change anything. The one exception is the polarization asymmetry A_1 , which shows a sensitivity to the employed potential at high, positive values of y .

We have also studied the influence of the p wave in the ground-state wave function on the observables. While most observables undergo only small shifts in peak position and small changes in peak height, our results do confirm the larger influence of the p -wave contribution on A_1 at large positive y values observed in Ref. [22]. However, the other observables seem to be fairly robust with respect to the p wave.

ACKNOWLEDGMENTS

The authors thank A. Radyushkin for a discussion clarifying a point he made in a talk, and M. Paris for discussions on his model calculations. S.J. thanks G. A. Miller for a discussion on numerical methods. This work was supported in part by funds provided by the U.S. Department of Energy (DOE) under cooperative research agreement under No. DE-AC05-84ER40150 and by the National Science Foundation under Grants No. PHY-0139973 and No. PHY-0354916.

[1] E. D. Bloom and F. J. Gilman, Phys. Rev. Lett. **25**, 1140 (1970); Phys. Rev. D **4**, 2901 (1971).

[2] I. Niculescu *et al.*, Phys. Rev. Lett. **85**, 1182 (2000); **85**, 1186 (2000); R. Ent, C. E. Keppel, and I. Niculescu, Phys.

- Rev. D **62**, 073008 (2000); S. Liuti, R. Ent, C.E. Keppel, and I. Niculescu, Phys. Rev. Lett. **89**, 162001 (2002).
- [3] Jefferson Lab Hall C E94-110 Collaboration, Y. Liang *et al.*, nucl-ex/0410027.
- [4] C.S. Armstrong, R. Ent, C.E. Keppel, S. Liuti, G. Niculescu, and I. Niculescu, Phys. Rev. D **63**, 094008 (2001).
- [5] Z.E. Meziani *et al.*, hep-ph/0404066.
- [6] J. Arrington, R. Ent, C.E. Keppel, J. Mammei, and I. Niculescu, nucl-ex/0307012; J. Arrington *et al.*, Phys. Rev. C **64**, 014602 (2001).
- [7] HERMES Collaboration, A. Airapetian *et al.*, Phys. Rev. Lett. **90**, 092002 (2003).
- [8] HERMES Collaboration, A. Fantoni *et al.*, Eur. Phys. J. A **17**, 385 (2003).
- [9] Jefferson Lab experiment E01-012, J.-P. Chen, S. Choi, and N. Liyanage, spokespersons.
- [10] "The Science Driving the 12 GeV Upgrade of CEBAF," edited by L. Cardman, R. Ent, N. Isgur, J.-M. Laget, C. Leemann, C. Meyer, and Z.-E. Meziani, White Paper, Jefferson Lab 2001.
- [11] F.E. Close and N. Isgur, Phys. Lett. B **509**, 81 (2001).
- [12] F.E. Close and W. Melnitchouk, Phys. Rev. C **68**, 035210 (2003).
- [13] F.E. Close and Q. Zhao, Phys. Rev. D **66**, 054001 (2002).
- [14] Q. Zhao and F.E. Close, Phys. Rev. Lett. **91**, 022004 (2003); hep-ph/0411257.
- [15] C.E. Carlson, hep-ph/0005169; A. Afanasev, C.E. Carlson, and C. Wahlquist, Phys. Rev. D **62**, 074011 (2000).
- [16] C.E. Carlson and N.C. Mukhopadhyay, Phys. Rev. D **58**, 094029 (1998); **47**, 1737 (1993); **41**, 2343 (1990).
- [17] Y.B. Dong and J. He, Nucl. Phys. A **720**, 174 (2003).
- [18] Y.B. Dong and M.F. Li, Phys. Rev. C **68**, 015207 (2003).
- [19] Y.B. Dong, Nucl. Phys. A **744**, 293 (2004); Y.B. Dong and J. Liu, Nucl. Phys. A **739**, 166 (2004); Y.B. Dong and Q.G. Feng, Commun. Theor. Phys. **39**, 675 (2003); Y.B. Dong and M.F. Li, Commun. Theor. Phys. **39**, 193 (2003).
- [20] M.W. Paris and V.R. Pandharipande, Phys. Lett. B **514**, 361 (2001); M.W. Paris, Eur. Phys. J. A **17**, 401 (2003); M.W. Paris and V.R. Pandharipande, Phys. Rev. C **65**, 035203 (2002).
- [21] M.W. Paris, Phys. Rev. C **68**, 025201 (2003).
- [22] V.R. Pandharipande, M.W. Paris, and I. Sick, nucl-th/0410093; V.R. Pandharipande, M.W. Paris, and I. Sick, nucl-th/0308078.
- [23] R. Fiore, A. Flachi, L.L. Jenkovszky, A.I. Lengyel, and V.K. Magas, Eur. Phys. J. A **15**, 505 (2002); L. Jenkovszky, V.K. Magas, and E. Predazzi, Eur. Phys. J. A **12**, 361 (2001).
- [24] A. Le Yaouanc, D. Melikhov, V. Morenas, L. Oliver, O. Pene, and J.C. Raynal, Phys. Lett. B **488**, 153 (2000).
- [25] G. Ricco, M. Anghinolfi, M. Ripani, S. Simula, and M. Taiuti, Phys. Rev. C **57**, 356 (1998); S. Simula, Phys. Lett. B **481**, 14 (2000).
- [26] W. Melnitchouk, Phys. Rev. Lett. **86**, 35 (2001); **93**, 199901(E) (2004).
- [27] W. Melnitchouk, K. Tsushima, and A.W. Thomas, Eur. Phys. J. A **14**, 105 (2002); F.M. Steffens and K. Tsushima, Phys. Rev. D **70**, 094040 (2004); K. Tsushima, K. Saito, and F.M. Steffens, hep-ph/0409217.
- [28] N. Isgur, S. Jeschonnek, W. Melnitchouk, and J.W. Van Orden, Phys. Rev. D **64**, 054005 (2001).
- [29] S. Jeschonnek and J.W. Van Orden, Phys. Rev. D **65**, 094038 (2002).
- [30] S. Jeschonnek and J.W. Van Orden, Phys. Rev. D **69**, 054006 (2004).
- [31] J.W. Van Orden and S. Jeschonnek, Eur. Phys. J. A **17**, 391 (2003).
- [32] M.A. DeWitt and S. Jeschonnek, prepared for the 17th Annual Hampton University Graduate Studies Program at CEBAF (HUGS 2002), Newport News, Virginia, 2002.
- [33] Z. Batiz and F. Gross, Phys. Rev. D **69**, 074006 (2004).
- [34] S. Liuti, Eur. Phys. J. A **17**, 397 (2003); N. Bianchi, A. Fantoni, and S. Liuti, Phys. Rev. D **69**, 014505 (2004).
- [35] V.V. Davidovsky and B.V. Struminsky, Yad. Fiz. **66**, 1368 (2003) [Phys. At. Nucl. **66**, 1328 (2003)]; hep-ph/0205130.
- [36] R. Hofmann, Prog. Part. Nucl. Phys. **52**, 299 (2004); Nucl. Phys. B **623**, 301 (2002).
- [37] R.F. Lebed and N.G. Uraltsev, Phys. Rev. D **62**, 094011 (2000).
- [38] See, e.g., I. Bigi and N. Uraltsev, Int. J. Mod. Phys. A **16**, 5201 (2001); I. Bigi, M. Shifman, N. Uraltsev, and A. Vainshtein, Phys. Rev. D **59**, 054011 (1999); B. Grinstein and R.F. Lebed, Phys. Rev. D **59**, 054022 (1999); **57**, 1366 (1998); C.G. Boyd, B. Grinstein, and A.V. Manohar, Phys. Rev. D **54**, 2081 (1996).
- [39] N. Isgur and M.B. Wise, Phys. Rev. D **43**, 819 (1991).
- [40] See, e.g., R. Rapp and J. Wambach, Adv. Nucl. Phys. **25**, 1 (2000).
- [41] M.A. Shifman, A.I. Vainshtein, and V.I. Zakharov, Nucl. Phys. B **147**, 448 (1979); **147**, 385 (1979); A.I. Vainshtein, V.I. Zakharov, V.A. Novikov, and M.A. Shifman, Sov. J. Nucl. Phys. **32**, 840 (1980); E.C. Poggio, H.R. Quinn, and S. Weinberg, Phys. Rev. D **13**, 1958 (1976); A.V. Radyushkin, in *Strong Interactions at Low and Intermediate Energies*, edited by J.L. Goity (World Scientific, Singapore, 2000); T.D. Cohen, R.J. Furnstahl, D.K. Griegel, and X. Jin, Prog. Part. Nucl. Phys. **35**, 221 (1995).
- [42] Minerva Collaboration, D. Drakoulakos *et al.*, hep-ex/0405002.
- [43] C.J. Horowitz, M.A. Perez-Garcia, and J. Piekarewicz, Phys. Rev. C **69**, 045804 (2004).
- [44] Vipuli Dharmawarda (private communication).
- [45] M. Diehl, Phys. Rep. **388**, 41 (2003).
- [46] H. Gao and L. Zhu, nucl-ex/0411014.
- [47] A. De Rújula, H. Georgi, and H.D. Politzer, Ann. Phys. (N.Y.) **103**, 315 (1977); Phys. Lett. **64B**, 428 (1977).
- [48] X. Ji and P. Unrau, Phys. Rev. D **52**, 72 (1995); Phys. Lett. B **333**, 228 (1994); X. Ji and W. Melnitchouk, Phys. Rev. D **56**, 1 (1997).
- [49] N. Isgur, Phys. Rev. D **59**, 034013 (1999).
- [50] Jefferson Lab Hall A Collaboration, X. Zheng *et al.*, Phys. Rev. C **70**, 065207 (2004).
- [51] M. Wakamatsu, Phys. Rev. D **67**, 034005 (2003); **67**, 034006 (2003).
- [52] Jefferson Lab Hall A Collaboration, X. Zheng *et al.*, Phys. Rev. Lett. **92**, 012004 (2004).
- [53] Spin Muon Collaboration, D. Adams *et al.*, Phys. Lett. B **357**, 248 (1995).

- [54] HERMES Collaboration, K. Ackerstaff *et al.*, Phys. Lett. B **404**, 383 (1997).
- [55] E143 Collaboration, K. Abe *et al.*, Phys. Rev. Lett. **78**, 815 (1997); E154 Collaboration, K. Abe *et al.*, Phys. Rev. Lett. **79**, 26 (1997).
- [56] E142 Collaboration, P.L. Anthony *et al.*, Phys. Rev. D **54**, 6620 (1996).
- [57] N. Liyanage (private communication).
- [58] J. Zeng, J. W. Van Orden, and W. Roberts, Phys. Rev. D **52**, 5229 (1995).
- [59] S. Godfrey and N. Isgur, Phys. Rev. D **32**, 189 (1985).
- [60] T. W. Donnelly and A. S. Raskin, Ann. Phys. (N.Y.) **169**, 247 (1986).
- [61] A. W. Thomas and W. Weise, *The Structure of the Nucleon* (Wiley-Vch, Germany, 2001).
- [62] B. W. Filippone and X. D. Ji, Adv. Nucl. Phys. **26**, 1 (2001).
- [63] CLAS Collaboration, R. Fatemi *et al.*, Phys. Rev. Lett. **91**, 222002 (2003).
- [64] M. Amarian *et al.*, Phys. Rev. Lett. **89**, 242301 (2002).
- [65] E155 Collaboration, P.L. Anthony *et al.*, Phys. Lett. B **493**, 19 (2000).